

Article

Microstructural Investigations of Weld Deposits from Manganese Austenitic Alloy on X2CrNiMoN22-5-3 Duplex Stainless Steel

Ion Mitelea ¹, Daniel Mutașcu ², Olimpiu Karancsi ², Corneliu Marius Crăciunescu ¹, Dragos Buzdugan ¹ and Ion-Dragos Uțu ^{1,*}

¹ Department of Materials and Fabrication Engineering, Politehnica University Timisoara, Bulevardul Mihai Viteazul nr.1, 300222 Timisoara, Romania; ion.mitelea@upt.ro (I.M.); corneliu.craciunescu@upt.ro (C.M.C.); dragos.buzdugan@upt.ro (D.B.)

² Department of Oral Implantology and Prosthetic Restorations on Implants, Victor Babes, University of Medicine and Pharmacy Timisoara, Eftimie Murgu Square, No. 2, 300041 Timisoara, Romania; daniel.mutascu@student.upt.ro (D.M.); karancsi.olimpiu@umft.ro (O.K.)

* Correspondence: dragos.utu@upt.ro

Abstract: Duplex stainless steels are materials with high performance under mechanical stress and stress corrosion in chloride ion environments. Despite being used in many new applications such as components for offshore drilling platforms as well as in the chemical and petrochemical industry, the automotive industry, etc., they face issues of wear and hardness that limit current applications and prevent the creation of new use opportunities. To address these shortcomings, it is proposed to develop a hardfacing process by a special welding technique using a universal TIG source adapted for manual welding with a pulsed current, and a manganese austenitic alloy electrode as filler material. The opportunity to deposit layers of manganese austenitic steel through welding creates advantages related to the possibility of achieving high mechanical characteristics of this steel exclusively in the working area of the part, while the substrate material will not undergo significant changes in chemical composition. As a result of the high strain hardening rate, assisted mainly by mechanical twinning, manganese austenitic alloys having a face-centered cubic crystal lattice (f.c.c) and low stacking fault energy ($SFE = 20\text{--}40 \text{ mJ/m}^2$) at room temperature, exhibit high wear resistance and exceptional toughness. Following cold deformation, the hardness of the deposited metal increases to 465 HV5–490 HV5. The microstructural characteristics were investigated through optical microscopy (OM), scanning electron microscopy (SEM), energy-dispersive X-ray analysis (EDX), X-ray diffraction (XRD), and Vickers hardness measurements (HV). The obtained results highlighted the feasibility of forming hard coatings on duplex stainless steel substrates.

Keywords: hardfacing; duplex stainless steel; welding; austenitic manganese alloy; microstructure



Citation: Mitelea, I.; Mutașcu, D.; Karancsi, O.; Crăciunescu, C.M.; Buzdugan, D.; Uțu, I.-D. Microstructural Investigations of Weld Deposits from Manganese Austenitic Alloy on X2CrNiMoN22-5-3 Duplex Stainless Steel. *Appl. Sci.* **2024**, *14*, 3751.
<https://doi.org/10.3390/app14093751>

Academic Editor: Eiji Tokunaga

Received: 8 April 2024

Revised: 25 April 2024

Accepted: 26 April 2024

Published: 27 April 2024



Copyright: © 2024 by the authors. Licensee MDPI, Basel, Switzerland. This article is an open access article distributed under the terms and conditions of the Creative Commons Attribution (CC BY) license (<https://creativecommons.org/licenses/by/4.0/>).

1. Introduction

Duplex stainless steels have a balanced microstructure of austenite and ferrite (approximately in equal proportions) in their equilibrium state. The most used ones are:

- Fe 23Cr 4Ni 0.1N (AISI 2304, UNS S32304),
- Fe 22Cr 5.5Ni 3Mo 0.15N (AISI 2205, UNS S32205), and
- 25Cr 5Ni 2.5Mo 0.17N Cu (AISI 2505).

The alloying elements in these steels promote either austenite or ferrite formation, expanding the temperature range in which one of the phases is stable.

The main alloying elements in duplex stainless steels include chromium and molybdenum, which promote ferrite formation, as well as nickel, carbon, nitrogen, and copper, which promote austenite formation [1–5].

Applications of these steels include [1,6–8]

- Components exposed to cavitation phenomena: hydromechanical equipment (rotors and blades of pumps and hydraulic turbines, ship propellers for maritime and river vessels).
- Offshore drilling platforms for oil and gas (drilling and processing equipment, etc.).
- Seawater desalination plants.
- Chemical and petrochemical industries.

Duplex stainless steels have a higher yield strength and tensile strength compared to standard austenitic stainless steels, and they also exhibit greater toughness than ferritic stainless steels. This allows for the reduction in thickness and weight of components or equipment made from these types of steels. The lower nickel content (an expensive element) compared to austenitic stainless steels justifies their economic efficiency.

Additionally, due to their high chromium content and the presence of other alloying elements such as nickel and molybdenum, duplex stainless steels exhibit superior resistance to pitting corrosion and stress corrosion cracking in chloride-containing environments compared to standard austenitic stainless steels (such as X5CrNi18-10 and X2CrNiMo17-12-2). Because of the reduced nickel content, the production cost of duplex stainless steels is lower than that of austenitic stainless steels. The presence of nitrogen in the chemical composition plays an important role in increasing mechanical strength characteristics, raising the temperature at which austenite begins to form from ferrite, and promoting the precipitation of chromium nitrides at the interfaces of ferrite grains—ferrite and ferrite-austenite.

The proportion of the two phases, austenite (A) and ferrite (F), can be widely modified depending on:

- The content of alloying elements.
- The heating temperature for solution treatment of intermetallic phases.

Moreover, the application of heat treatments triggers the following phenomena with consequences for microstructure changes [1]:

- Precipitation of carbides such as $M_{23}C_6$ and nitrides such as Cr_2N at the grain boundary of ferrite-austenite, without consequences regarding intergranular corrosion.
- Light precipitation of the σ phase (from ferrite) during heating.
- Hardening through annealing treatments at temperatures ranging between 400 and 900 °C.

The main disadvantage of duplex stainless steels is related to their hardness and low resistance to wear through friction and cavitation erosion, factors that shorten the lifespan of component parts [8–12]. When covered with hardening alloys, these steels not only suffer from sensitization to the precipitation of chromium carbides $M_{23}C_6$, as is the case with austenitic stainless steels, but they are also susceptible to embrittlement due to the formation of secondary phases, i.e., intermetallics, carbides, and nitrides, as a result of prolonged exposure to high temperatures. Significant precipitation of secondary phases can lead to a loss of corrosion resistance and, sometimes, hardness loss.

From the perspective of hardfacing through welding, the greatest disadvantage of these steels is that when subjected to the typical thermal cycle of a coating process (temperatures of 300–1000 °C), they readily and quickly form a variety of fragile phases such as sigma (σ), chi (χ), and alpha-prime (α') [6–9]. This is practically unavoidable because during hard loading through welding, a thin portion of the surface of the piece melts, and even if the majority of the material remains below 300 °C, there is always an intermediate microzone (near the deposited layer-substrate interface) that will experience temperatures in the embrittlement range, even if only for a short period.

To avoid precipitation phenomena, it is necessary to maintain the temperature between two successive passes at approximately 150–200 °C. This ensures that the time spent in the embrittlement zone is minimized.

In recent years, numerous research efforts have been undertaken to modify the microstructure of the surface layers of these steels in order to increase hardness and improve

resistance to wear through friction and cavitation erosion. Among these, examples include laser beam welding, TIG welding, thermal spraying, and plasma nitriding.

Thus, Murad A. H. I. et al. investigated the effect of TIG (GTAW) and CO₂ laser beam welding (LBW) processes on the dimensions, microstructure, mechanical properties, and corrosion resistance of welded joints of duplex stainless steel, grade 2205 [13]. The results showed that LBW, compared to GTAW, provides better corrosion resistance (corrosion rate is 0.05334 mm/year for LBW and 0.2456 mm/year for GTAW). The explanation for these differences is based on the smaller dimensions of the welded joint and the heat-affected zone in the case of LBW welding.

Mridha S., Dyuti S. [14] demonstrated that by preplacing Ti powders on the surface of steel and subsequently remelting with TIG welding of the marginal layer, hardness increases to approximately 2000 HV due to the formation of TiN compounds, thus justifying the reduction in wear rate.

Lailatula H., Maleque M.A. [15] have shown that by TIG melting of the surface or by applying thermochemical gas nitriding treatment, significant surface hardening of duplex stainless steels is achieved, which promotes improvement in wear and corrosion resistance.

Paijan L. H. et al. [16] and Nagatsuka K. et al. [17] established that gas nitriding at temperatures of 400 °C–500 °C for 6 h in plasma leads to an increase in the hardness of duplex stainless steels to values exceeding 650 HV. The formation of expanded austenite was observed in the temperature range of 400 °C–500 °C, and chromium nitrides appearing at 500 °C decreases corrosion resistance.

The expansion of the potential applications of duplex stainless steels to parts operating under conditions of frictional wear and cavitation erosion has led the authors of this study to characterize the microstructure of coatings made of Fe-C-Mn-Cr-Ni alloys of the "Citomanganese" type deposited by arc welding with pulsed current. These alloys were developed based on Hadfield steels and are delivered in the form of powders, tubular wires, and coated electrodes. Because they have a high capacity for work hardening, they are recommended for use in hardfacing through welding of valves, shafts, and other components in industries such as automotive, aerospace, petrochemical, and metallurgical, which are subjected to intense wear stresses during operation [18–24].

Based on our knowledge, there are currently no available reports regarding the microstructure and hardness of the coating-substrate system under hardfacing of duplex stainless steels with austenitic manganese alloys using the manual shielded metal arc welding technique with pulsed current.

2. Materials, Experimental Procedure

The base material used as a substrate was duplex stainless steel 2205, symbolized as X2CrNiMoN22-5-3 according to the European standard EN 10088 and UNS S31803 according to ASTM A276. Before the hardfacing process, it underwent a solution annealing heat treatment at a temperature of 1060 °C followed by rapid cooling in water.

Table 1 presents the nominal chemical composition of this steel (determined by optical emission spectrometry using Thermo Arl QuantoDesk equipment from Thermo Fisher Scientific, Burladingen, Germany), and Table 2 shows the obtained values for the main mechanical characteristics at room temperature (determined using the equipment Zwick/Roell Z005, Ulm, Germany).

The selected filler material was the CITOMANGAN electrode with a basic coating of austenitic manganese steel, symbolized DIN 8555: ~E 7—UM—200 KP, and EN 14700: E Fe 9, respectively, which is recommended for deposition of wear-resistant layers under conditions of strong impacts and shocks. The guaranteed chemical composition of the deposited metal is as follows: 0.60% C, 15% Mn, 4.5% Cr, 4.8% Ni, and balance Fe.

Using a universal welding source MAGIC WAVE 300, from Fronius company, which allows, as an option, manual welding with pulsed current electrodes (Figure 1), depositions of 1, 2, or 3 layers of austenitic manganese steel (electrode) were made on the considered steel substrates. The novelty lies in the fact that in the welding torch head, in its grip, instead

of the non-fusible tungsten electrode, the selected coated electrode for hardfacing was fixed. Welding by melting with the electric arc in pulsed current differs from conventional welding in that the welding current varies over time between a maximum value called the pulse current and a minimum value called the base current, at a certain frequency (Figure 1).

Table 1. The chemical composition of the analyzed steel substrate.

Carbon (C)	0.021%
Silicon (Si)	0.79%
Manganese (Mn)	0.82%
Phosphorous (P)	0.019%
Sulfur (S)	0.012%)
Chromium (Cr)	22.34%
Nickel (Ni)	5.61%
Nitrogen (N)	0.14%
Molybdenum (Mo)	3.1%
Iron (Fe)	Balance

Table 2. Mechanical characteristics for the hyper-quenched state.

Yield strength, $R_{p,0.2}$ [N/mm ²]	545
Ultimate tensile strength, R_m [N/mm ²]	736
Elongation at break, A5 [%]	28
Necking, Z [%]	52
Hardness, HV [daN/mm ²]	275

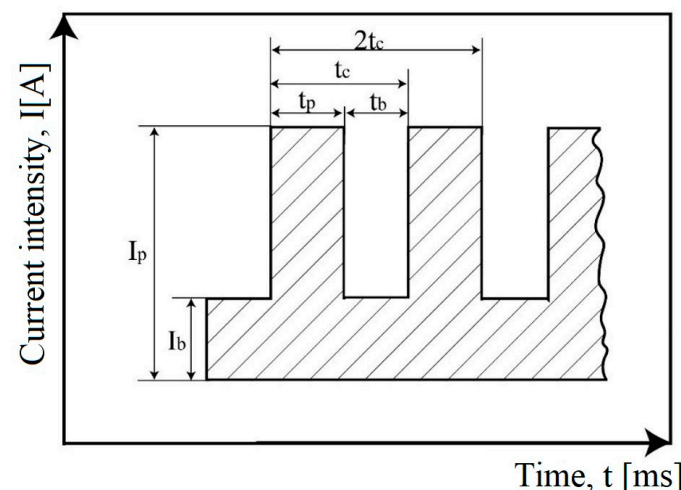


Figure 1. The parameters of the pulsed current welding process.

By adjusting the level of specific parameters: I_p , I_b , t_p , t_b , and f , it is possible to precisely dose the energy introduced into the components of the coating-substrate system. Melting of the material and formation of the weld bath occurs during a pulse, while stable burning of the electric arc is maintained during the base time, resulting in cooling with partial solidification of the molten bath. At the same average welding current, the penetration of the weld beam is greater than in conventional welding, and the linear energy is lower.

Through preliminary trials and based on data obtained from literature, the following conditions for carrying out the welding process in pulsed current were established:

- Basic coated electrode: CITOMANGAN;
- Electrode diameter: 3.25 mm;
- Polarity: DC+;
- Pulse current, I_p : 180 A;

- Base current, I_b : 90 A (50% of I_p);
- Average current, I_m : 135 A;
- Arc voltage, U : 22 V;
- Pulse frequency, $f = 1/t_c = 5$ Hz;
- Cycle time, $t_c = 1/f = 1/5 = 0.2$ s;
- Pulse time, $t_p = 0.5 t_c = 0.1$ s;
- Base time, $t_b = 0.5 t_c = 0.1$ s ($t_p = t_b$);
- Arc length, $l_a = 3.0$ mm;
- Welding rate, $v = 27\text{--}28$ cm/min.

Before welding hardfacing, the substrate surface was grinded with 120 gr SiC paper and cleaned with acetone. After each deposited layer, the surface was cleaned using a wire brush.

In all cases, the deposition of the first layer was performed in air, while maintaining the temperature of the samples in the range of 150–200 °C. For samples with two or three layers, the deposition of the second and third layers occurred after immersing them in water, considering the welding behavior of the austenitic manganese steel.

Immediately after welding deposition, the surface was hammered (struck) for a duration of 3–5 min using a pneumatic hammer. Subsequently, cross-sectional sections of the deposited layers were taken, and metallographic preparation was performed through grinding, polishing, and chemical etching operations. Grinding was performed up to SiC-P2500 paper, polishing up to 0.25 μm with diamond paste, and chemical etching was carried out using the Vilella reagent (10 g copper chloride, 30 mL HCl, and 120 mL distilled water). The average thickness of the first deposited layer was approximately 2 mm; and for the second and third layer, it was 1.5–1.8 mm each.

Microstructural characterization of the cross-sectional sections was conducted through optical microscopy (Leica DM2700M optical microscope from Leica Mikrosysteme Vertrieb GmbH, Wetzlar, Germany), scanning electron microscopy, energy-dispersive X-ray analysis (TESCAN VEGA 3 LMU scanning electron microscope with Bruker EDX Quantax from Bruker, Billerica, MA, USA), and X-ray diffraction analysis (Panalytical X'Pert Powder, Panalytical, The Netherlands).

Macrohardness Vickers (on the Zwick/Roell YHV-S apparatus, Ulm, Germany) with an applied force of 5 kgf (HV5) was determined based on measurements distributed on the cross-sectional sections of the coating-substrate system, which were ground with SiC-P4000, with a distance of 1.0 mm between each penetration depth and a holding time of 10 s.

3. Evaluation of Experimental Results

3.1. Macrographic Examinations

Although the welding deposition operation ensures material continuity, the welded area does not exhibit a homogeneous structure. As a result of heating, melting of the filler material, partial melting of the base material (BM), and subsequent cooling, various structural transformations occur.

Macroscopic examinations of the samples hardfaced under the specified technological conditions aimed the geometry of the depositions and any defects such as porosity and cracks. For these investigations, samples were sectioned perpendicular to the deposition. After grinding with metallographic paper CarbiPro Silicon Carbide Abrasive Paper from 60 grit to 1200 grit and further polished with diamond suspension from 9 to 1 μm, the samples were chemically etched with the Villela reagent.

In Figure 2, macroscopic images of samples hardfaced with one, two, and three layers are presented. These images highlight the corresponding geometry of the deposited metal (layer) zone and the absence of material continuity defects. Since austenitic steel does not exhibit polymorphic transformations, it is not possible to achieve a fine-grain finish in the heat-affected zone (HAZ), and the large grains resulting from each pass seem to impede each other's growth.

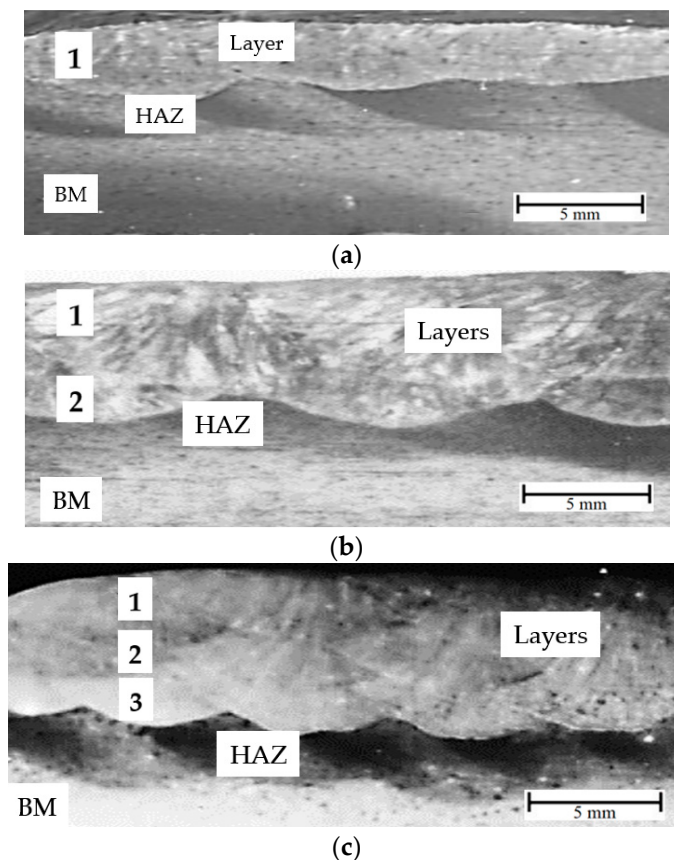


Figure 2. Macrographic images of the layer—substrate system: (a) one layer deposited; (b) two layers deposited; (c) three layers deposited.

3.2. Micrographic Examinations

These are detailed investigations that allow for the assessment of the quality of the deposited layers and provide indications for optimizing the hardfacing welding process. The microstructure of the solution heat treatment of the base metal was assessed by quantitative metallographic determinations with a Fischer feritscope (DMP 30 equipment from Berg Engineering & Sales Company, Inc., Rolling Meadows, IL, USA) and is composed of approximately 48% ferrite and 52% austenite (Figure 3).

In Figure 4, the microscopic image of the deposited metal–base metal interface during the deposition of a single layer is rendered. As a result of the melting of the filler material and a small portion of the substrate material, a weld bath is formed. The solidification process ensures good bonding between the two materials, and defects such as pores and cracks are absent. In the lower part of the deposited material (towards the base material, BM), a dendritic microstructure oriented strongly in the direction of the thermal gradient appears, a phenomenon explainable by the rapid cooling rate from the high temperature reached during welding. The development of crystalline grains in the melted zone from pre-existing grains is called epitaxial growth. During pulsed current welding, the heat input into the samples is lower than in conventional electric arc welding, and the cooling rate is increased. Consequently, the proportion of carbides precipitated in the interface zone, a phenomenon due to the diffusion tendency of carbon from the deposited material (DM) to the base material, is limited. It is known that if the cooling rate from the peak temperature reached during welding is higher, the degree of undercooling is higher, the critical radius of crystallization nuclei is smaller, the number of nuclei is higher, and the resulting structure is finer.

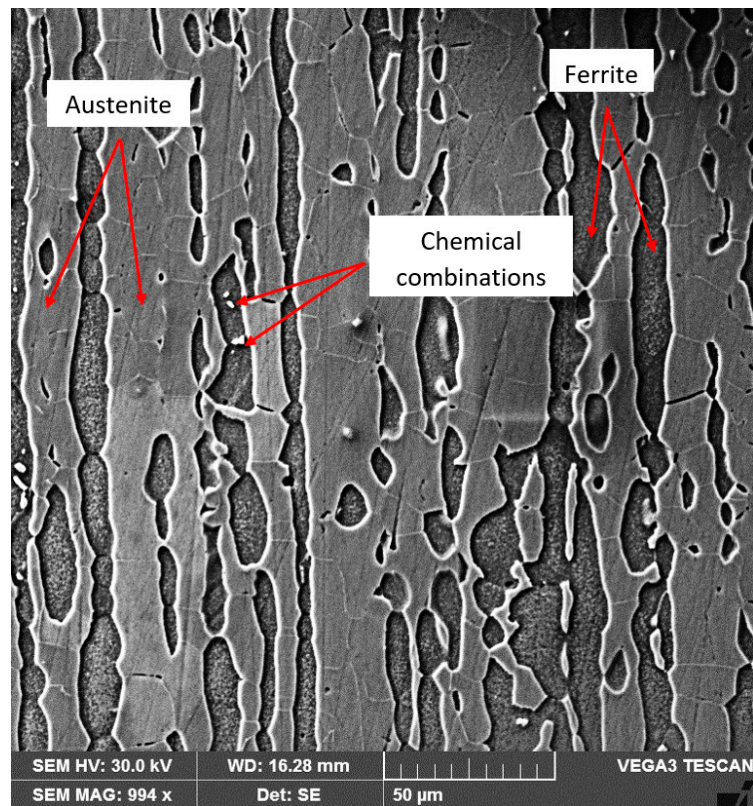


Figure 3. The microstructure of the base metal.

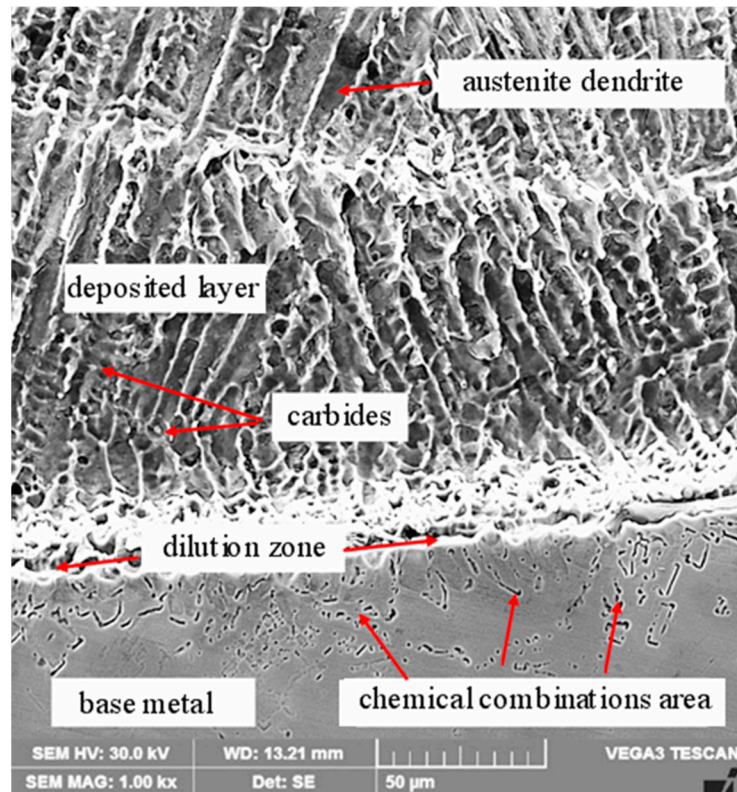


Figure 4. Micrograph of the MD–MB interface at the deposition of the first layer.

As solidification progresses, the upper part of the coating develops a cellular-dendritic microstructure in which the presence of secondary phases can be observed (see Figure 5).

The phenomena of precipitation of secondary phases such as carbides are somewhat less intense because a significant portion of the heat generated during welding is absorbed by the water in which the majority of the base metal mass was placed.

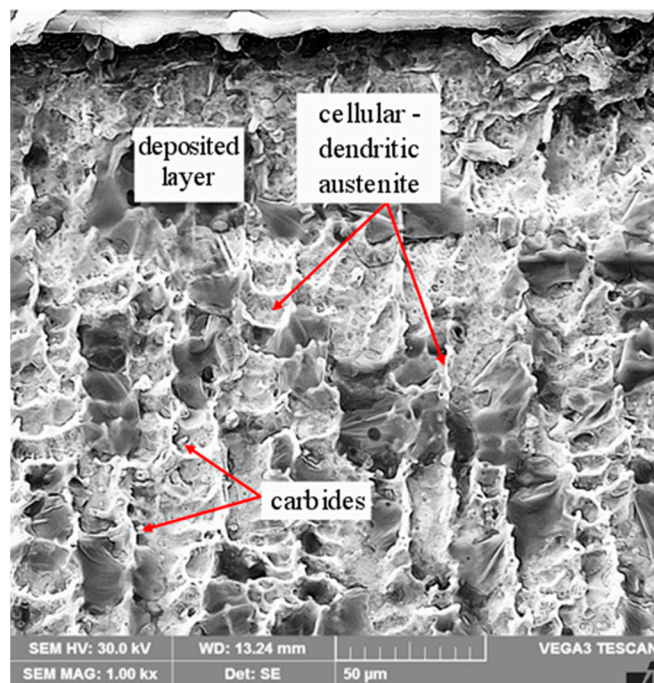


Figure 5. Micrograph of the outer layer deposited by hardfacing welding.

The presented microstructural images characterize the weld-deposited metal layers without subsequent hammering applied for internal stress relaxation. It has been previously shown that the primary characteristic of the deposited metal from this steel is its high sensitivity to work hardening. If correct surface hammering is carried out after the deposition of each layer (under the instructions provided in Figure 6), significant increases in hardness and important modifications in the microstructural features will be observed.

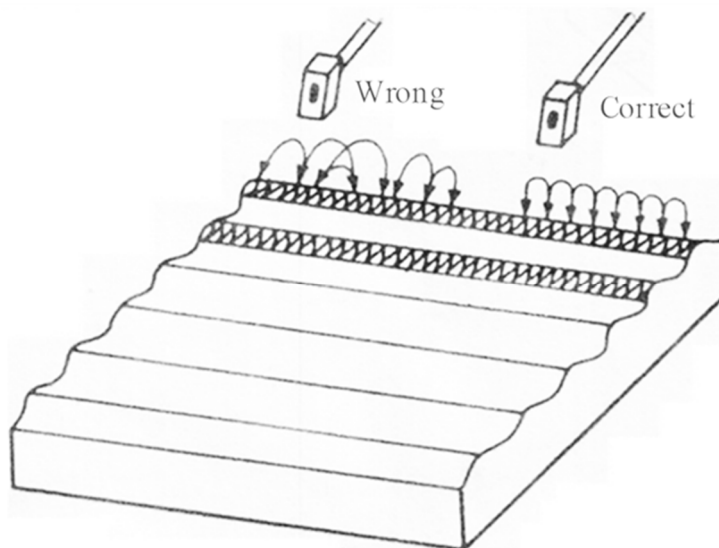


Figure 6. Modes of hammering the deposited layer.

To avoid the danger of cracking in deposited layers under the action of internal stresses, it is always recommended to reduce them by surface hammering. Under the action of local deformations, stress relaxation occurs, thus reducing the risk of cracking.

Figure 6 presents an example of internal stress relaxation through hammering, applied incorrectly on the left and correctly on the right. The operation involves delivering blows with constant amplitudes, at the same frequency (2–3 Hz), as well as maintaining constant and uninterrupted paths. The deformation time was 4 min with continuous and uniform movement of the chisel over the entire surface, alternating the hammering direction at a 90-degree angle after each pass. Another method to reduce the risk of cracking in the deposited layer is based on inducing compressive stresses in the deposited layer by welding on a pre-tensioned surface.

Figure 7 confirms the high capacity of the deposited metal for work hardening. On one hand, fragmentation of the dendritic structure is observed, while on the other hand, the appearance of twins and ϵ -martensite is noted. Additionally, the precipitation phenomena of fine carbide particles intensify, exhibiting a uniform distribution in the deposited metal zone, (DM), Figure 5, particularly near its interface with the base metal (BM), Figure 4, and oriented towards the direction of ϵ -martensite or twins, in other regions of the DM. These microstructural observations are in full agreement with the results of other research studies [18–24].

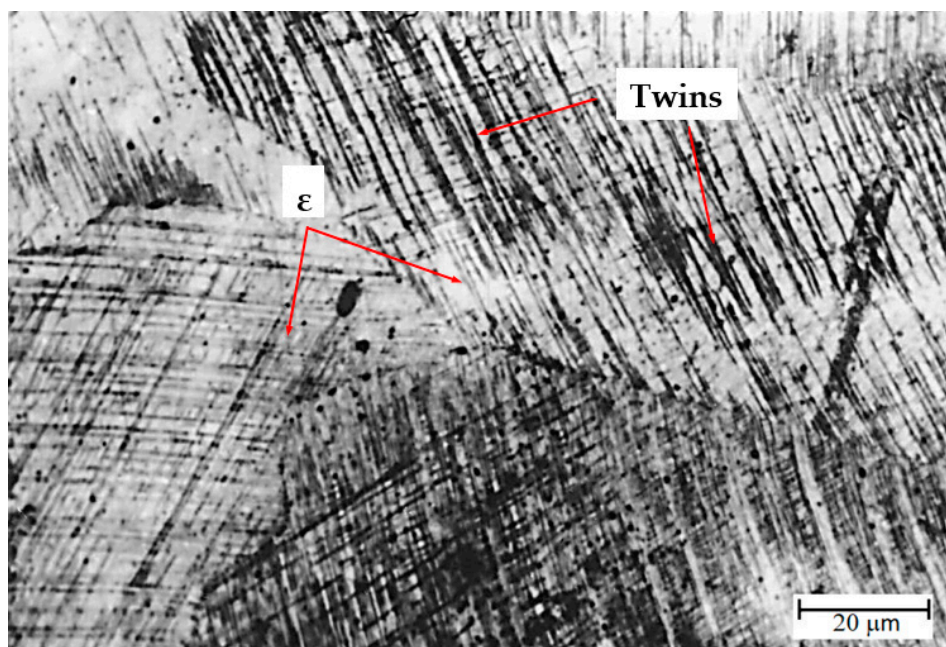


Figure 7. Optical micrographic image ($\times 1000$) of the work-hardened layer.

In the microstructure of work hardened deposited metal, alongside the base matrix, which is austenite, a certain proportion of martensite ϵ is observed. This phase (white needles) is located along the slip lines and especially at their intersections. The ϵ phase is a known microstructure from the Fe-Mn binary alloy system, for concentrations of 12 . .30% Mn, and it can transform through long-term heat treatment or cold deformation into the α phase [18,19,23,24].

3.3. EDX Analyses: The Degree of Dilution

The hardfacing welding process is accompanied by penetration of the component elements of the substrate material into the first layer of deposited metal. Therefore, the dilution of the deposited layer occurs due to mixing with the melted substrate, affecting its functional properties to some extent. It is worth noting that dilution increases with the increase in linear energy during welding. The measurement of the degree of dilution was

conducted through chemical composition analysis using energy-dispersive X-ray analysis (EDX) (see Figure 8). The calculation relationship is as follows:

$$Gd = (Fe_{wm} - Fe_{fm}) / (Fe_{bm} + Fe_{fm}) \times 100 = (81.02 - 75.10) / (65.27 + 75.10) \times 100 = 4.2\%$$

where

Gd is the degree of dilution;

Fe_{wm} is the iron content in the deposited layer, mass %;

Fe_{fm} is the iron content in the filler material, mass %;

Fe_{bm} is the iron content in the base material, mass %.

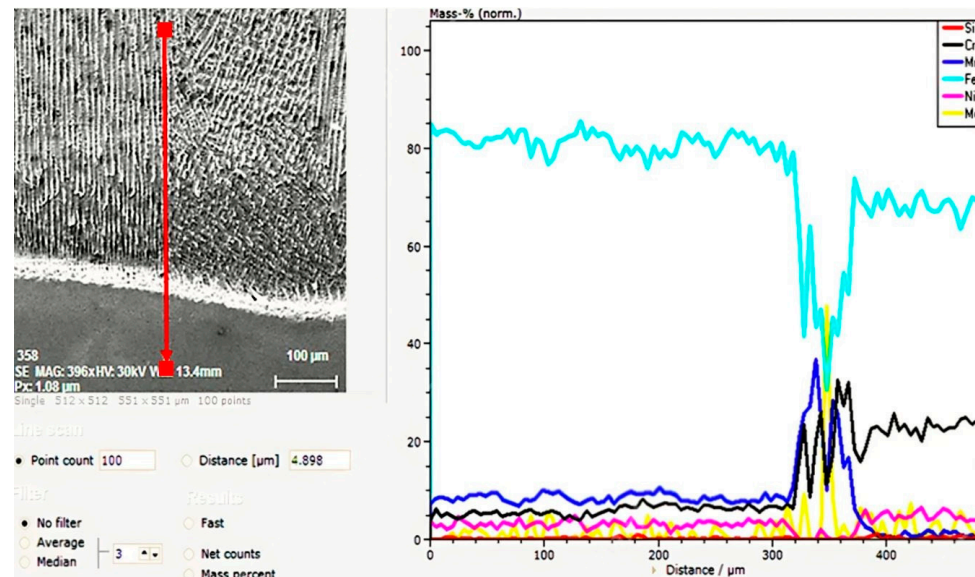


Figure 8. SEM image and the concentration profiles of the alloying elements on one side and the other of the interface between the deposited metal and the base metal.

The low value of the dilution degree provides an efficient control of the deposited metal properties, in correlation with the intended purpose. Conducting the welding process in pulsed current offers the possibility of unlimited adjustment of the technological regime parameters, thus limiting the heat input introduced into the base material.

3.4. X-ray Diffraction

X-ray diffraction (XRD) analysis characterized the secondary phases precipitated during solidification and solid-state transformations. The investigations were conducted using a Panalytical X’Pert Powder X-ray spectrometer equipped with a graphite monochromator for Cu-K α radiation ($\lambda = 1.54$ Å), at room temperature. The scanning details applied in these analyses were: 2Theta range from 20 to 100 degrees, with a step size of approximately 0.03 degrees and counting at each step for 2 s. Cu K α radiation was used, and the power of the X-ray generator was set to 40 kV and 30 mA. For indexing the interference peaks, the X’Pert High Score software version 5.0 and its database were used. Figures 9 and 10 show two characteristic X-ray diffraction patterns for the substrate and the first layer of deposited metal. It is noteworthy that in the substrate, the two characteristic phases of any duplex stainless steel (austenite and ferrite) are present, while in the vicinity of the first deposited layer, additional particles of complex carbides of alloying elements are observed.

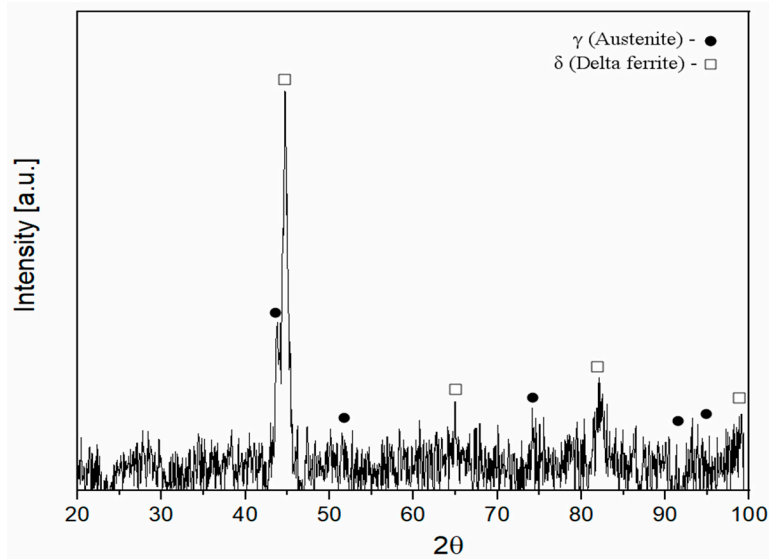


Figure 9. X-ray diffraction pattern of the substrate.

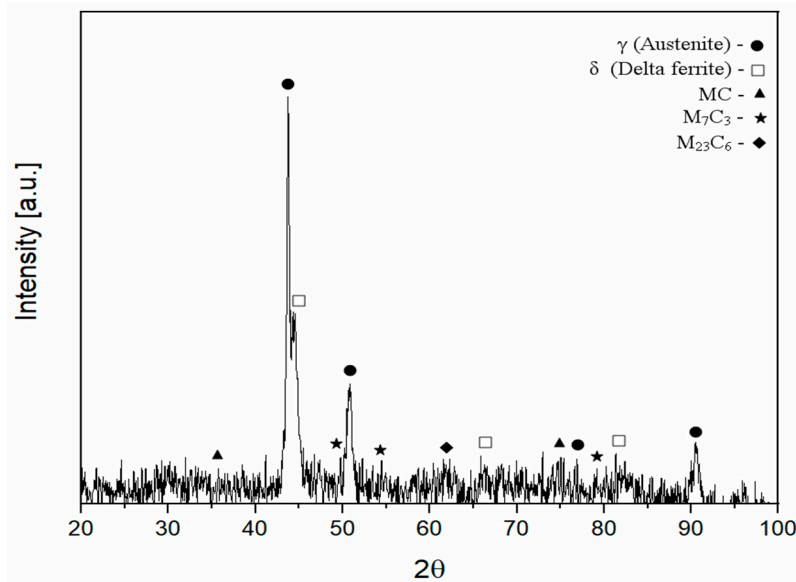


Figure 10. X-ray diffraction pattern of the layer microzone near the interface with the substrate material.

3.5. Hardness Measurements

Since hardness values are most sensitive to microstructural changes induced by the thermal welding cycle, such measurements were made on sections taken in a direction perpendicular to the deposits.

The influence exerted by structural and chemical composition changes at various depths of the coating and substrate was highlighted through measurements of Vickers hardness. Figure 11 presents the hardness gradient curve on the ground and polished cross-section, from the top of the deposited layer to the substrate. It is notable that due to dilution, the hardness of the first deposited layer is 300 HV5–360 HV5, while the subsequent layers, unaffected by dilution, vary between 465 HV5 and 490 HV5. In the solution annealing heat-treated base metal, the hardness values range from 264 HV5–282 HV5.

The presence of a small amount of carbides in the upper part of the coating did not decrease the crack resistance because the achieved hardness level is not very high.

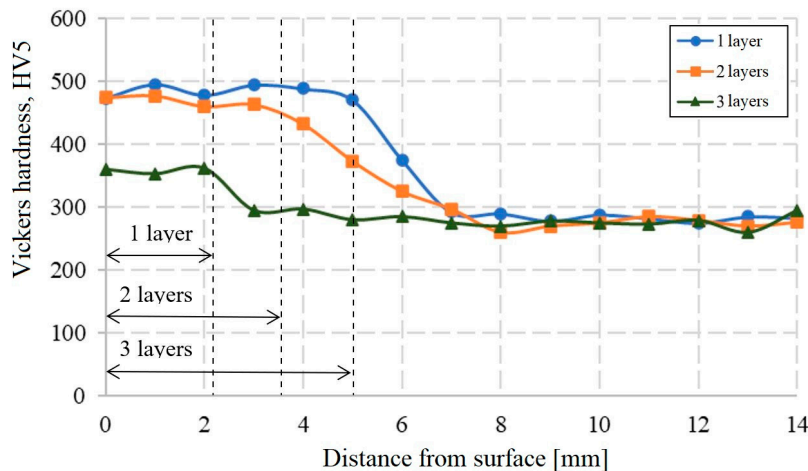


Figure 11. Hardness gradient curve on the cross-section of the layer-substrate system.

4. Conclusions

Based on the results obtained and presented in this study regarding the microstructural characteristics of layers of manganese austenitic alloys deposited by manual electric arc welding in pulsed current on duplex stainless steels, the following conclusions have been drawn:

- The welding process parameters ensure a reduction in the heat input into the components and an increase in the cooling rate, thus limiting the degree of dilution and the precipitation phenomena of carbide phases. Consequently, the dimensions and proportion of carbides are smaller.
- Macroscopic examination shows that the coatings were strongly bonded to the substrate, without continuity defects, indicating good metallurgical adhesion.
- Following surface work hardening, the hardness of the first deposited layer, affected by dilution, ranges from 355 HV5 to 365 HV5, while that of the second and third deposited layers reaches 468 HV5–492 HV5.
- The microstructure of the last deposited layer is austenitic with a cellular-dendritic character and a small proportion of carbides, as a large part of the heat generated during welding is absorbed by the water in which the largest mass of base material was placed.

Author Contributions: Conceptualization, I.M. and I.-D.U.; methodology, I.M., D.M., C.M.C. and I.-D.U.; investigation, I.M., D.M., C.M.C., O.K., D.B. and I.-D.U.; writing—original draft preparation, I.M., D.M. and I.-D.U.; writing—review and editing, I.M., C.M.C., O.K., D.B. and I.-D.U.; visualization, I.M., D.M., C.M.C., O.K., D.B. and I.-D.U.; supervision, I.M.; project administration, I.M.; funding acquisition, C.M.C. All authors have read and agreed to the published version of the manuscript.

Funding: This project is supported by a grant from the Romanian Ministry of Education and Research, CNCS-UEFISCDI, project number PN-IV-P1-PCE-2023-1425.

Institutional Review Board Statement: Not applicable.

Informed Consent Statement: Not applicable.

Data Availability Statement: Data are contained within the article.

Acknowledgments: I.M. and C.M.C acknowledge, as members, the support from the Technical Sciences Academy of Romania.

Conflicts of Interest: The authors declare no conflict of interest.

References

- Charles, J. Past, present and future of duplex stainless steel. In Proceedings of the La Paine Saint Denis, France—Duplex Conference, Paris, France, 29 May 2007; pp. 1–10.
- Badji, R.; Bouabdallah, M.; Bacroix, B.; Kahloun, C.; Belkessa, B.; Maza, H. Phase transformation and mechanical behavior in annealed 2205 duplex stainless steel welds. *Mater. Charact.* **2008**, *59*, 447–453. [[CrossRef](#)]
- Yang, Y.; Yan, B.; Li, J.; Wang, J. The effect of large heat input on the microstructure and corrosion behaviour of simulated heat affected zone in 2205 duplex stainless steel. *Corros. Sci.* **2011**, *53*, 3756–3763. [[CrossRef](#)]
- Kai, W.; Chan, K.W.; Tjong, S.C. Effect of Secondary Phase Precipitation on the Corrosion Behavior of Duplex Stainless Steels. *Materials* **2014**, *7*, 5268–5304. [[CrossRef](#)] [[PubMed](#)]
- Jiang, Y.; Tan, H.; Wang, Z.; Hong, J.; Jiang, L.; Li, J. Influence of C_{req}/Ni_{eq} on pitting corrosion resistance and mechanical properties of UNS S32304 duplex stainless steel welded joints. *Corros. Sci.* **2013**, *70*, 252–259. [[CrossRef](#)]
- Sadeghian, M.; Shamanian, M.; Shafyei, A. Effect of heat input on microstructure and mechanical properties of dissimilar joints between super duplex stainless steel and high strength low alloy steel. *J. Mater. Des.* **2014**, *60*, 678–684. [[CrossRef](#)]
- Rowlands, B.S.; Rae, C.; Galindo-Navarrete, E. The Portevin-Le Chatelier effect in nickel-base superalloys: Origins, consequences and comparison to strain ageing in other alloy systems. *Prog. Mater. Sci.* **2023**, *132*, 101038. [[CrossRef](#)]
- Al-Hashem, A.; Riad, W. The effect of duplex stainless steel microstructure on its cavitation morphology in seawater. *Mater. Charact.* **2001**, *47*, 389–395. [[CrossRef](#)]
- Karimi, A.; Karimipour, A.; Akbari, M.; Mehdi Razzaghi, M.; Ghahderijani, M.J. Investigating the mechanical properties and fusion zone microstructure of dissimilar laser weld joint of duplex 2205 stainless steel and A516 carbon steel. *Opt. Laser Technol.* **2023**, *158 Pt A*, 108875. [[CrossRef](#)]
- Kwok, C.T.; Man, H.C.; Cheng, F.T. Cavitation erosion of duplex and super duplex stainless steels. *Scr. Mater.* **1998**, *39*, 1229–1236. [[CrossRef](#)]
- Karimi, A. Cavitation erosion of a duplex stainless steel. *Mater. Sci. Eng.* **1987**, *86*, 191–203. [[CrossRef](#)]
- Wu, Y.; Lian, Y.; Li, Y.; Feng, M. Cavitation Erosion Behavior of 2205 and 2507 Duplex Stainless Steels in Distilled Water and Artificial Seawater. *Tribol. Online* **2023**, *18*, 482–493. [[CrossRef](#)]
- Murad, A.H.I.; Khourshid, A.; Sharef, T. Gas tungsten arc and laser beam welding processes effects on duplex stainless steel 2205 properties. *Mater. Sci. Eng.* **2012**, *549*, 105–113. [[CrossRef](#)]
- Mridha, S.; Dyuti, S. Effect of processing parameters on microstructure and properties TIG melted surface layer of steel. *Adv. Mater. Res.* **2011**, *264–265*, 1421–1426. [[CrossRef](#)]
- Lailatula, H.; Maleque, M.A. Hardfacing of duplex stainless steel using melting and diffusion processes. *IOP Conf. Ser. Mater. Sci. Eng.* **2017**, *184*, 012030. [[CrossRef](#)]
- Paijan, L.H.; Berhan, M.N.; Adenan, M.S.; Yusof NF, M.; Haruman, E. Structural development of expanded austenite on duplex stainless steel by low temperature thermochemical nitriding process. *Adv. Mater. Res.* **2012**, *576*, 260–263. [[CrossRef](#)]
- Nagatsuka, K.; Nishimoto, A.; Akamatsu, K. Surface hardening of duplex stainless steel by low temperature active screen plasma nitriding. *Surf. Coat. Technol.* **2010**, *5*, 5295–5299. [[CrossRef](#)]
- Zambrano, O.A. A general perspective of Fe–Mn–Al–C steels. *J. Mater. Sci.* **2018**, *53*, 14003–14062. [[CrossRef](#)]
- Koyama, M.; Sawaguchi, T.; Tsuzaki, K. Overview of dynamic strain aging and associated phenomena in Fe–Mn–C austenitic steels. *ISIJ Int.* **2018**, *58*, 1383–1395. [[CrossRef](#)]
- Müller, A.; Segel, C.; Linderov, M.; Vinogradov, A.; Weidner, A.; Biermann, H. The portevin–Le Châtelier effect in a metastable austenitic stainless steel. *Metall. Mater. Trans.* **2016**, *47*, 59–74. [[CrossRef](#)]
- Lee, S.-J.; Kim, J.; Kane, S.N.; De Cooman, B.C. On the origin of dynamic strain aging in twinning-induced plasticity steels. *Acta Mater.* **2011**, *59*, 6809–6819. [[CrossRef](#)]
- Jiang, M.; Huang, C.; Qian, L.; Jia, P.; Huang, R.; Li, L. Physical properties of a high manganese austenitic steel Fe-30%Mn-1%C at cryogenic temperatures. *Cryogenics* **2023**, *129*, 103629. [[CrossRef](#)]
- Wang, P.; Ren, J.; Chen, Q.; Chen, J.; Liu, Z. Effect of secondary twins on strain hardening behavior of a high manganese austenitic steel at 77 K by quasi in situ EBSD. *Mater. Charact.* **2021**, *180*, 111428. [[CrossRef](#)]
- Yuan, X.; Chen, L.; Zhao, Y.; Di, H.; Zhu, F. Influence of annealing temperature on mechanical properties and microstructures of a high manganese austenitic steel. *J. Mater. Process. Technol.* **2015**, *217*, 278–285. [[CrossRef](#)]

Disclaimer/Publisher’s Note: The statements, opinions and data contained in all publications are solely those of the individual author(s) and contributor(s) and not of MDPI and/or the editor(s). MDPI and/or the editor(s) disclaim responsibility for any injury to people or property resulting from any ideas, methods, instructions or products referred to in the content.